Effects of micro-alloying Ag on microstructure, mechanical properties and corrosion behavior of extruded Mg-2Zn-0.2Ca-xAg alloys

Jie Yin[a], Miao Li[b], Fang Yi[c], Xingjian Zhao[d], Dikai Guan[d], Kaicheng Wang[a], Yonghao Gao[a*], Chuming Liu[a]

a. School of Materials and Engineering, Central South University, Changsha 410083, China
b. Beijing Institute of Remote Sensing Equipment, Beijing, 100071
c. Hunan Xiangya Stomatological Hospital, Central South University, Changsha 410000, China
d. Department of Mechanical Engineering, School of Engineering, University of Southampton, Southampton, SO17 1BJ, UK

ABSTRACT

The present work investigates effects of micro-alloying Ag on the microstructure, mechanical properties and corrosion behavior of as-extruded Mg-2Zn-0.2Ca alloys. The addition of Ag, up to 0.5 wt.%, induce limited difference on microstructural characteristics such as slightly coarser microstructures due to the enhanced dynamic recrystallization process and the presence of refined precipitates. The tensile properties of the alloy were not significantly changed by Ag addition, i.e., all the alloys exhibited exceptional elongation of ~30%, moderate tensile yield strength and ultimate strength of ~140 MPa and ~240 MPa, respectively. The corrosion performance of the alloys was progressively deteriorated with increasing Ag content i.e., the corrosion rate increased from 0.40 ± 0.23 mm/y for Mg-2Zn-0.2Ca alloy to 3.27 ± 0.24 mm/y for the Mg-2Zn-0.2Ca-0.5Ag alloy. The compromised corrosion performance was attributed to a large electrode potential difference between the nobler $Ca_2Mg_6Zn_3$ phase and the α-Mg matrix as well as a less protective corrosion film, by increasing Ag addition.

Keywords: Magnesium Alloys; Mg-Zn-Ca-Ag; Microstructure Characterization; Corrosion Behavior; Mechanical Properties

* Corresponding author: gaoyonghao_009@163.com, gaoyonghao@csu.edu.cn

1. Introduction

As the population ages, an increasing number of individuals will become susceptible to various degenerative diseases, such as arthritis, osteoporosis, and trauma. This trend has sparked a significant global demand for orthopedic implants [1, 2]. Magnesium (Mg) based alloys have attracted considerable attention as implant materials due to their outstanding biocompatibility, elastic modulus closer to natural bone (compared with bio-inert metals like titanium, stainless steel and cobalt-chromium alloys), and unique biodegradability without the need for a second extraction surgery [1]. Nevertheless, the rapid degradation of magnesium alloys can result in premature failure before the completion of the healing process, limiting their application. Therefore, the development of biocompatible magnesium alloys with superior mechanical properties as well as controllable degradation rate is crucial [1].

Many magnesium alloys have been developed to explore their feasibility for biomedical applications, of which Mg-Zn-Ca-based alloys attract increasing attention because of their excellent biocompatibility and high mechanical properties [3-9]. Zinc emerges as the most crucial alloying element, enhancing mechanical properties of Mg alloys through both solution strengthening and precipitation hardening, while minimizing the degradation rate by eliminating adverse effects of impurities in Mg alloys [8, 10, 11]. A biodegradable Mg-2.0Zn alloy had been clinically approved and its composition was further optimized by adding a small amount of calcium [3, 12], considering that Ca, an essential biological element, helps improving tensile strength and reducing the corrosion rates of Mg-Zn based alloys by refining microstructure [5, 13]. For example, it was found that a minor (0.2 wt.%) amount of Ca increased the tensile yield strength (TYS) of a Mg-2Zn alloy by 115 MPa [12] and reduced the corrosion rate of a Mg–2Zn–0.5Mn alloy by ~ 20% [5].

The incorporation of silver (Ag), a well-known antimicrobial agent, into Mg alloys was reported to enhance their antibacterial activity [14-17], which is considered beneficial to eliminate postoperative infections. Additional advantages induced by Ag addition to Mg includes promoting secondary phase precipitation to strengthen Mg alloys and

reducing *c*/*a* ratio to the improve their ductility and deformability [18, 19]. For example, the tensile elongation of a Mg-Zn alloy was significantly increased from 12.0% to 19.8% with a minor (0.2 wt.%) addition of Ag [18].

Based on both the strengthening effects as well as the bio-functionality of Zn, Ca and Ag, quaternary Mg-Zn-Ca-Ag alloys have been extensively studied for developing of biodegradable Mg alloys [17, 20]. Optimizing the composition, especially the Ag content, of the quaternary alloy is not an easy task, as inconsistent results have been reported on how Ag could affect the biodegradation behavior of the magnesium alloys. Some publications reported that adding Ag into Mg based alloys deteriorated their corrosion performance [16, 18, 21, 22], while Ag was also reported to improve their corrosion resistance [14, 20]. Moreover, it seems that the corrosion resistance of the Mg-Zn-Ca alloys may either be improved or deteriorated depending on Ag content. For instance, Yu et al. [20] added different amounts of Ag into a Mg-3Zn-0.2Ca alloy, and found that an addition of 0.3 wt.% Ag yielded the optimum result in terms of reduced biodegradation. Dragomir et. al. [14] claimed that a minimum of 2.5 wt.% Ag is needed to improve the corrosion resistance of a biodegradable Mg-Zn alloy, which is contrary to the results reported by Ma et al. [22] that the Ag content of >2 wt.% severely compromised the corrosion resistance of the Mg-1Zn-0.2Ca alloy.

The inconsistency in the literatures on the effects of the Ag addition to the degradation behavior of the Mg-Zn-Ca alloy motivates us to explore further this area. In the present study, different amounts of Ag were added to a Mg-2.0Zn-0.2Ca, a clinically approved biodegradable Mg alloy, to comparatively investigate their microstructure characteristics, mechanical properties and corrosion performances.

2. Materials and methods

2.1 Materials preparation

Pure Mg (99.95 wt.%), pure Zn granules (99.995 wt.%) and Mg-25 wt.% Ca master alloy were initially melted at approximately 740 °C in a steel crucible. Subsequently, the temperature of the melt was raised to about 780 °C to facilitate the dissolution of

pure Ag (99.99 wt.%). The melt was then thoroughly refined to get a homogenized composition. Throughout the entire smelting process, the molten alloy was shielded by a flux to prevent burning. The melt was then cooled to 680 ^{o}C and transferred to the DC casting unit to produce ingots. Actual compositions of the prepared ingots were evaluated using inductively coupled plasma optical emission spectroscopy (ICP-OES, Spectro Blue Sop, Germany), the detection limit was better than 1 ppm, with a resolution of 16 picometers (pm) and an accuracy better than 0.5%. The chemical compositions of the studied alloys are summarized in Table 1.

Table 1 Actual chemical composition of the studied alloys (wt.%).

Alloy Designation	Alloying Elements				Impurity Elements			
	Mg	Zn	Ca	Ag	Fe	Cu	Ni	Si
ZX20	*Bal.*	2.00	0.20	-	0.0110	0.0013	0.0008	0.0110
ZXQ0.1	*Bal.*	2.07	0.20	0.11	0.0047	0.0006	0.0028	0.0073
ZXQ0.3	*Bal.*	2.00	0.20	0.27	0.0083	0.0006	0.0004	0.0150
ZXQ0.5	*Bal.*	2.04	0.17	0.50	0.0091	0.0006	0.0027	0.0092

2.2 Microstructure characterization

The microstructural analysis of investigated alloys, both before and after corrosion, was conducted using scanning electron microscopy (SEM, Tescan Mira3, Czech) equipped with an energy dispersive spectroscopy detector (EDS). The grain size and orientation information were acquired using an Oxford Instruments C-Nano electron backscatter diffraction (EBSD) detector embedded in the SEM facility with a step size of 0.5 μm. The area fraction of the secondary phases in as-extruded alloys were obtained by analyzing corresponding SEM images using ImageJ software. Phase composition of the studied alloys was evaluated by X-ray diffraction (XRD) using a D/Max 2500VB diffractometer with Cu K_{α} radiation (λ=0.154 nm) operated in the Bragg-Brentano geometry. The diffraction was conducted in a 2θ range of 20^{o}-80^{o} with a scanning rate of 1 ^{o}/min, and a step size of 0.02^{o}. The acquired XRD patterns were then analyzed using the simple search / match function incorporated in the MDI Jade Pro software (with PDF-4+ diffraction files). The surface potential of polished samples was examined by scanning Kelvin probe force microscopy (SKPFM) using a Bruker Dimension Icon instrument. All measurements were performed at room temperature in atmospheric conditions maintained with 40% relative humidity. The sample

microstructure was also characterized using a FEI Talos F200S transmission electron microscope (TEM) with an accelerating voltage of 200 kV. As-extruded samples were initially ground using progressively finer SiC papers up to 3500 grit, followed by polishing with silica suspension for SEM characterization. The EBSD sample preparation involved further electropolishing at a voltage of 25 mV in a perchloric acid solution at -35 ^{o}C. The TEM specimen preparation involved mechanical grounding, twin-jet electropolishing (using a solution of 95 vol% alcohol and 5 vol% perchloric acid at -35 °C). The sample was finally thinned using a Gatan 691 ion thinner, by bombardment with energetic Ar ions of 3 keV from a 3° cutting angle.

2.3 Uniaxial tensile and compression tests

The mechanical properties of as-extruded alloys along the extrusion direction (ED) were determined through both tensile and compression tests. Tensile testing was conducted in accordance with ASTM E8 specification using an Instron 3369 universal testing machine with a tension rate of 2 mm/min. The gauge section in the tensile sample had a length of 25 mm and a diameter of 5 mm. For compression testing, the samples were cylindrical with dimensions of ∅8 mm×16 mm, and the compression rate was 1 mm/min. Triple tests were performed to ensure the reliability and validity of the results.

2.4 Immersion tests

The corrosion behavior of the samples was evaluated using both immersion tests and electrochemical techniques. The samples for immersion tests were cut from as-extruded rods into dimensions of 10 mm × 10 mm × 5 mm. Prior to corrosion test, the samples were ground using 3500 grit SiC papers, ultrasonically cleaned in ethyl alcohol and finally dried in blowing air. All samples were immersed in 0.9 wt.% NaCl solution for 15 days at a temperature of 37 ± 1 ^{o}C. During the immersion test, hydrogen bubbles released from the sample surface were collected, which volume of gas evolved quantified using an inverted burette [23], and the corrosion rate was calculated using Equation (1) in accordance with ASTM F3268-18a:

$$P_H = 2.279 V_H \quad (1)$$

where V_H (mL·cm^{-2}·day^{-1}) is the hydrogen evolution rate estimated by recording the volume of water expelled from the burette at intervals of 12 hours. After immersion test, the samples were sequentially washed using chromic acid, water, and ethyl alcohol to remove the corrosion products. The weight loss (ΔW) in the immersion was also converted into corrosion rate according to the Equation (2) in accordance with ASTM G31-12a:

$$P_W = \frac{8.76 \times 10^4 \times \Delta W}{A \times D \times T} \quad (2)$$

where ΔW (g) represents the weight loss of specimens following immersion, A (cm^2) is the surface area of specimens, D (g·cm^{-3}) is the density of alloys and T (h) is the immersion time.

2.5 Electrochemical measurements

Electrochemical measurements were conducted in 0.9 wt.% NaCl solution by using a three-electrode cell comprising a sample as the working electrode, a platinum plate as the counter electrode and a saturated calomel electrode (SCE) as the reference electrode. The exposed surface area of each sample was 10 mm×10 mm. After 2 hours immersion, the open circuit potential (OCP) was stabilized to allow the potentio-dynamic polarization (PDP) tests that were performed by scanning in the range of -300 ~ +300 mV (*vs.* OCP) with a rate of 1 mV·s^{-1}. Electrochemical impedance spectroscopy (EIS) was carried out after stabilization of the OCP value, with perturbation amplitude of 5 mV in the frequency range from 10^5 to 10^{-2} Hz.

3. Results and discussion

3.1. Microstructure evolution after hot extrusion

Fig. 1 displays SEM images of as-extruded alloys. The microstructure of all samples comprised fine equiaxed grains and a limited number of elongated grains (Fig. 1(a-d)). After Ag addition, the number of elongated grains reduced, and the size of equiaxed grains increased, especially noticeable when the Ag content reached 0.5 wt.%. Furthermore, the coexistence of coarse intermetallic along extrusion direction (ED) (Fig. 1(a-d)) with fine intermetallic primarily located at grain boundaries and

moderately within grains (Fig. 1(e-f)), was also observed. The coarse intermetallics might have originated from the residual secondary phase after homogenization, while the fine intermetallic might result from dynamic precipitation during hot extrusion. Notably, all samples exhibited similar intermetallic volume fractions, approximately 1.2%, except that a fraction of ~0.8% was determined in the alloy containing 0.5 wt.% Ag.

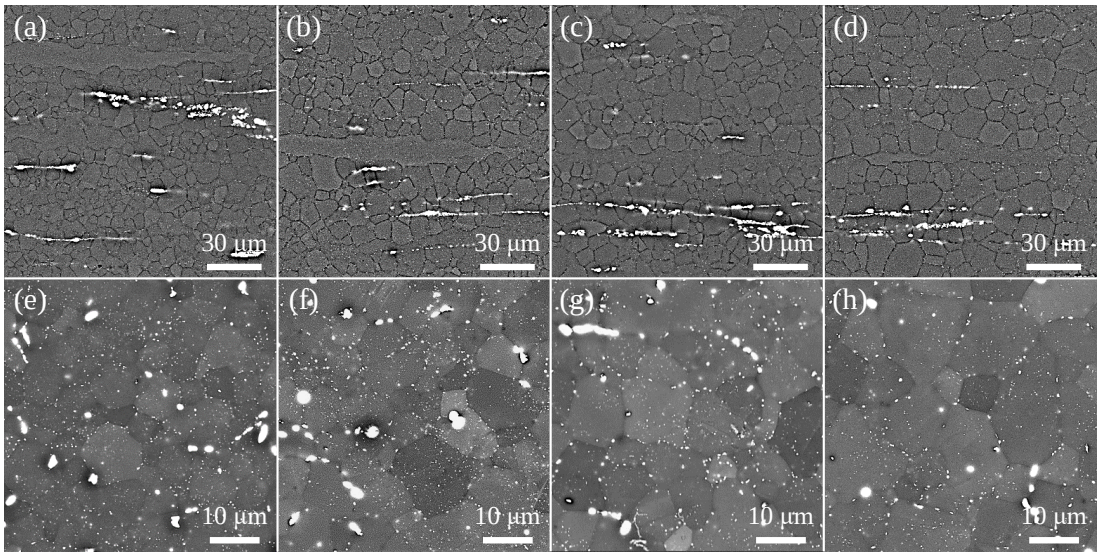

Fig. 1. Backscattered electron SEM images of the longitude (a~d) and transverse (e~h) sections of as-extruded Mg-2Zn-0.2Ca-xAg (x=0, 0.1, 0.3 and 0.5 wt.%) alloys: (a, e) ZX20, (b, f) ZXQ0.1, (c, g) ZXQ0.3 and (d, h) ZXQ0.5.

Chemical composition of the intermetallic was analyzed using EDS, and the results are depicted in Fig. 2 and listed in Table 2. It is evident that both Zn and Ca are concentrated in the secondary phases of as-extruded alloys. Notably, the addition of Ag did not alter the distribution of Zn and Ca. Co-segregation of Ag with Zn and Ca in the secondary phase was identified by a noticeably higher Ag content in those regions compared to the surrounding α-Mg matrix (Table 2). Moreover, Ag concentration in the intermetallic gradually increased with the rising Ag content in the alloy. Specifically, Ag content in the secondary phases of the ZXQ0.1 alloy was measured at 0.3 at.% (Region 4 in Fig. 3(b)), increasing gradually to 0.7 at.% (Region 6 in Fig. 3(c)) and 1.3 at.% (Region 8) for the ZXQ0.3 and ZXQ0.5 alloys, respectively. The consumption of Ag in the secondary phases reduced its concentration in the α-Mg matrix, and Ag was even undetectable in the α-Mg matrix of the ZXQ0.1 and ZXQ0.3 alloys when the bulk Ag

addition was apparently low. The atomic Zn/Ca ratio in the secondary phases of the alloys was calculated to vary around the stoichiometric 3/2 ratio in the intermetallic $Ca_2Mg_6Zn_3$. Therefore, the secondary phase observed in the alloy was preliminarily determined as $Ca_2Mg_6Zn_3$ as reported elsewhere [9, 12]. Additionally, there were minor traces of Ca-rich intermetallics in the ZX20 and ZXQ0.5 alloys (Region 2 and 9 in Fig. 3), although their fraction was low enough to be neglected in the present study.

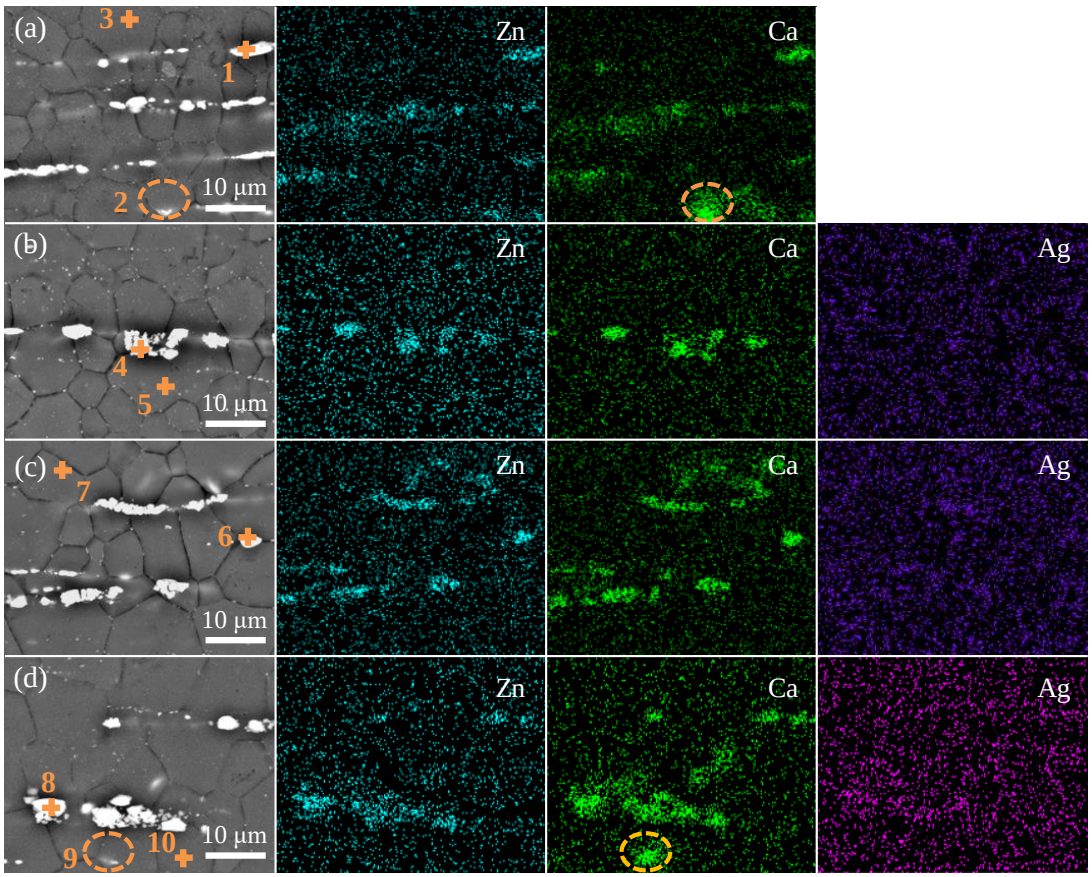

Fig. 2. SEM-EDS mapping results of as-extruded Mg-2Zn-0.2Ca-xAg (x=0, 0.1, 0.3 and 0.5 wt.%) alloys: (a) ZX20, (b) ZXQ0.1, (c) ZXQ0.3 and (d) ZXQ0.5.

Table 2 EDS results (at.%) from matrix and the second phase particles in as-extruded Mg-2Zn-0.2Ca-xAg (x=0, 0.1, 0.3 and 0.5 wt.%) alloys of Fig. 2.

Elements	ZX20			ZXQ0.1		ZXQ0.3		ZXQ0.5		
	1	2	3	4	5	6	7	8	9	10
Mg	82.0	83.5	99.2	82.8	99.0	80.2	99.3	78.1	91.7	99.0
Zn	11.7	2.5	0.7	10.6	1.0	11.9	0.6	12.0	2.9	0.7
Ca	6.2	14.0	0.1	6.2	0.1	7.2	0.1	8.7	5.2	0.2
Ag	-	-	-	0.3	-	0.7	-	1.3	0.3	0.1

Fig. 3 illustrates the XRD results of as-extruded alloys. The coexistence of α-Mg and $Ca_2Mg_6Zn_3$ phases was observed in all the specimens. The presence of the α-Mg phase

was straightforward, while the $Ca_2Mg_6Zn_3$ phase was determined by the diffraction peaks at 2θ=21.1° and 2θ=41.2°. Consistent with EDS analysis, small additions of Ag did not induce any new phases in the alloy. The relative intensity of the peaks associated with the $Ca_2Mg_6Zn_3$ phase decreased with increasing Ag content, particularly evident in the ZXQ0.5 alloy.

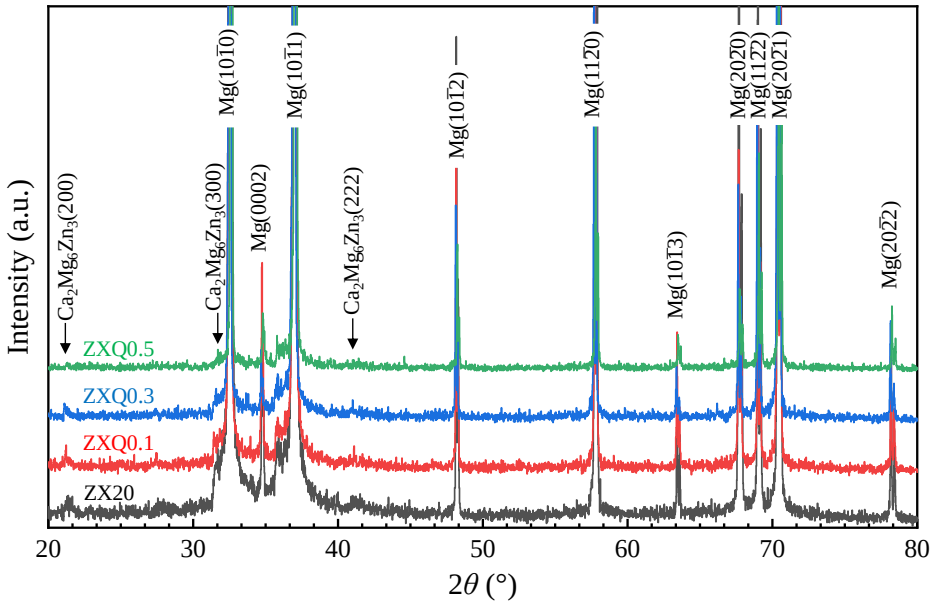

Fig. 3. XRD patterns of as-extruded Mg-2Zn-0.2Ca-xAg (x=0, 0.1, 0.3, 0.5 wt.%) alloys.

Fig. 4 displays TEM images, selected area electron diffraction (SAED) patterns, and elemental distributions of as-extruded ZX20 and ZXQ0.3 alloys. In line with the results shown in Fig. 1, fine intermetallics distributed within the grains and at the grain boundaries in both the Ag-free and Ag-containing alloys. Notably, the precipitates situated at grain boundaries exhibited larger dimensions than those within the grains. This size discrepancy was attributed to a higher energy of grain boundaries, leading to preferential segregation of solute atoms and subsequent formation of larger precipitates [24]. The area fraction of precipitates in the ZX0.3 alloy was, 1.1 ± 0.3%, slightly lower than that of ZX20 (1.2 ± 0.3%). Chemical analysis of the secondary phases was conducted to reveal co-segregation of Zn, Ca and Ag in the secondary phases (Fig. 4 and Table 3). The SAED indexing results depicted in Figure 4, along with the chemical analysis outlined in Table 3, determined further that the secondary phases observed in the ZX20 and ZXQ0.5 alloys were $Ca_2Mg_6Zn_3$, consistent with those documented in [9].

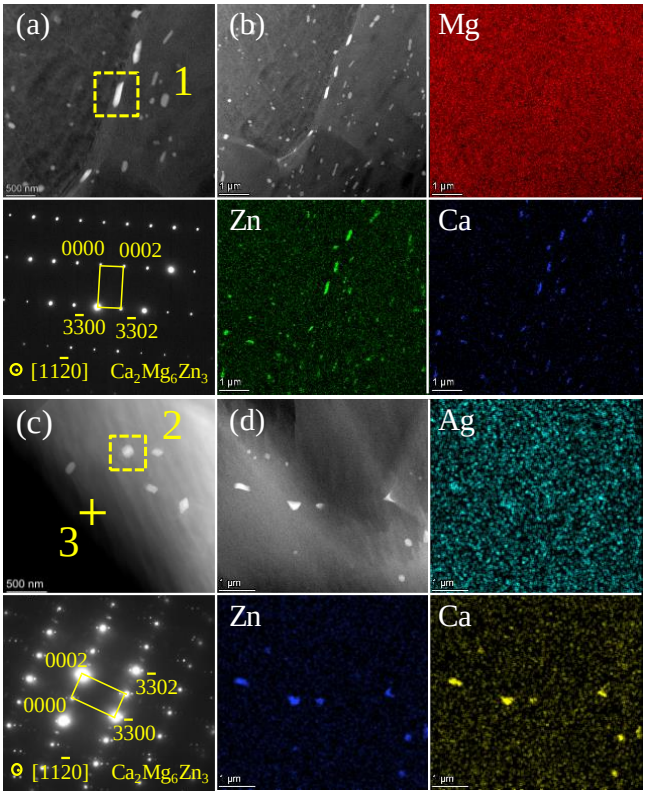

Fig. 4. Higher magnification dark field images (a, c) with corresponding selected-area electron diffraction (SAED) images of the precipitates of yellow box, lower magnification dark field images and corresponding EDS mappings (b, d): ZX20 (a, b) and ZXQ0.3 (c, d).

Table 3 EDS results (at.%) collected from the points marked in Fig. 4.

Elements	ZX20	ZXQ0.5	
	1	2	3
Mg	85.92	73.14	99.22
Zn	10.28	17.05	0.09
Ca	3.80	9.09	0.02
Ag	-	0.72	0.09

Fig. 5 represents the inverse pole figure (IPF) maps as well as the (0002) pole figures of as-extruded alloys. Consistent with the SEM images shown in Fig. 1, as-extruded alloys comprised mainly fine equiaxed grains and minor elongated grains. After analyzing the grain orientation spreads (GOS) following widely accepted criteria [25], the fine equiaxed grains possessing a GOS of <2° were considered to be formed through the dynamic recrystallization (DRX) process during hot extrusion, and therefore, assigned as DRXed grains. On the other side, the elongated grains possessed high GOS values (GOS>2°) were determined to be deformed grains.

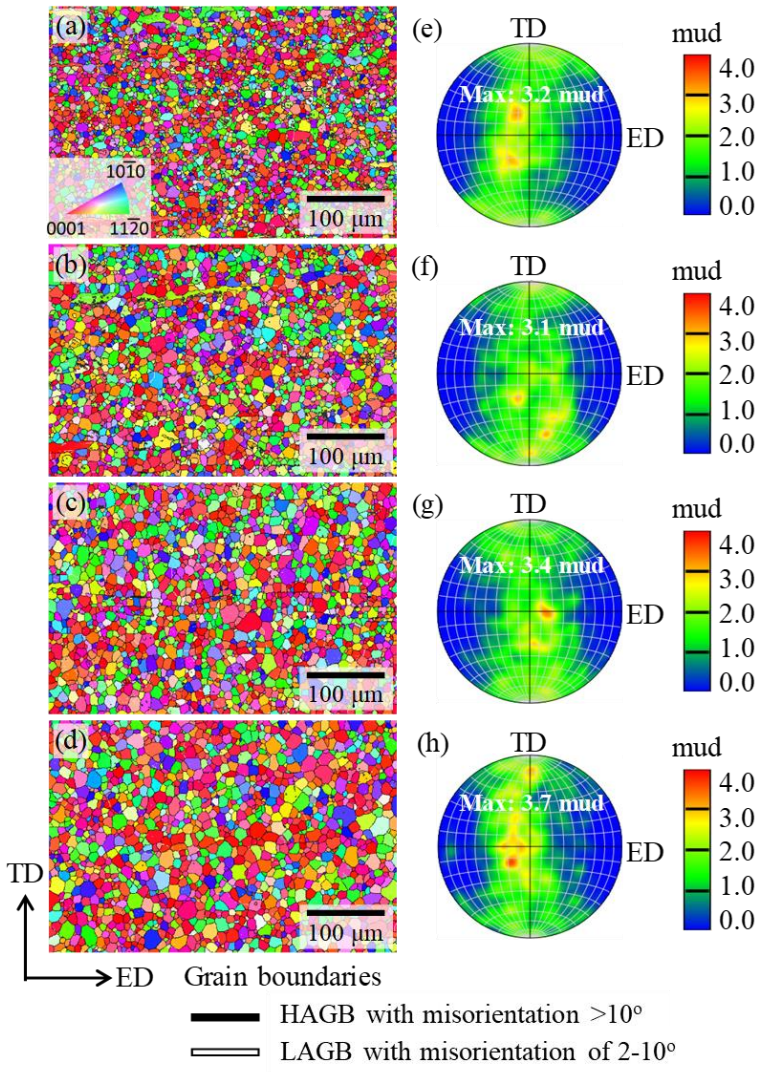

Fig. 5. EBSD inverse pole figure (IPF) maps (a~d) and corresponding (0002) pole figures (e~h) of as-extruded Mg-2Zn-0.2Ca-xAg (x=0, 0.1, 0.3 and 0.5 wt.%) alloys: (a, e) ZX20, (b, f) ZXQ0.1, (c, g) ZXQ0.3, (d,h) ZXQ0.5.

The volume fraction of DRXed grains (V_{DRX}), as well as their average grain size (AGS) were calculated, and the results are summarized in Fig. 6. All samples had been recrystallized to a high extent with V_{DRX} values higher than 90%. Moreover, a trend for V_{DRX} to increase along with the Ag content was also confirmed. To be specific, the V_{DRX} value increased slightly from 90.6% to more than 93.7%, for the ZX20 and ZXQ0.5 alloy, respectively. Meanwhile, the AGS values of the two alloys were measured to be 8.7 ± 2.8 μm and 13.8 ± 4.6 μm, respectively. These observations suggested that Ag addition promoted the DRX process and facilitated subsequent grain growth. According to the (0002) pole figure (Fig. 5), all as-extruded samples exhibited rather similar texture characteristics, with a similar maximum pole intensity among them, irrespective

of the Ag content in the alloy. To be specific, each of as-extruded alloys exhibited a typical fiber texture, characterized by the majority of grains aligning their *c*-axis (<0001> direction) perpendicular to ED, albeit spreading unevenly in the radial directions.

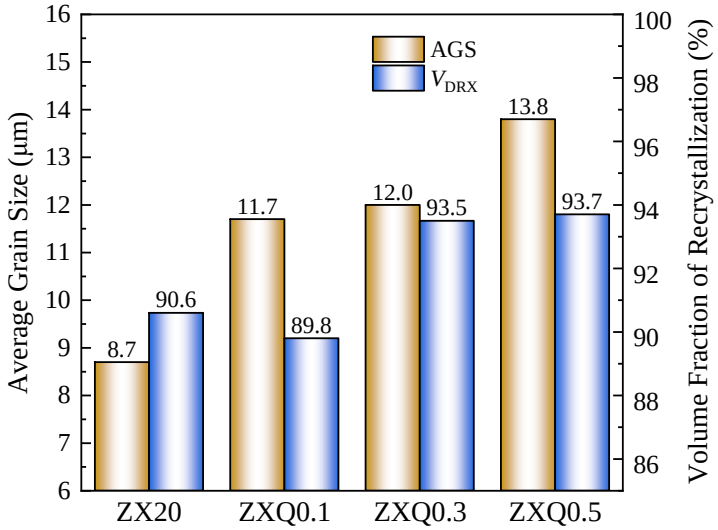

Fig. 6. Comparison of V_{DRX} and AGS values among as-extruded Mg-2Zn-0.2Ca-xAg (x=0, 0.1, 0.3 and 0.5 wt.%) alloys.

3.2 Tensile and compression properties

Fig. 7 depicts the engineering stress-strain curves obtained from both tensile and compression tests of the as-extruded alloys at room temperature. Whilst the curves in Fig. 7 were derived from a single experiment, the mean average results of three parallel tests are summarized in Table 4. All the samples exhibited conventional hardening type stress-strain tensile curves. The stress corresponding to a 0.2% strain was considered as the yield strength. All specimens exhibited exceptional fracture elongation (FE) around 30%，in tensile test, irrespective of the Ag content. Nevertheless, Ag addition slightly reduced the TYS of the alloys, while the ultimate tensile strength (UTS) maintained roughly the same (~240 MPa). The reduction in TYS was primarily attributed to coarsening the microstructure (Fig. 5-6) which compromised the precipitation strengthening effect due to lower amounts of the secondary phase particles (Fig. 1). The ZX20 alloy exhibited the highest strength and considerable ductility under the tensile tests, with the values of TYS, UTS and FE being approximately 151.5 MPa, 244.1 MPa and 29.9% respectively.

On the other hand, the compressive stress-strain curves possessed sigmoidal shapes

with significant yielding plateau related to the deformation twinning [26]. In contrast to that observed in tensile tests, the introduction of Ag resulted in a moderate enhancement in the strength and fracture strain of as-extruded alloys during compression tests. A dramatically higher yield strength was derived in tension compared to compression (Fig. 7 and Table 4), irrespective of the Ag contents in the alloys, exhibiting the typical yielding asymmetry of highly textured Mg alloys [27, 28]. Notably, the ultimate compressive strength increased from 361.8 ± 13.0 MPa to 381.9 ± 7.8 MPa, and the fracture strain increased from 18.6 ± 0.8% to 21.1 ± 2.2% when 0.5 wt.% Ag was added to the Mg-Zn-Ca alloy.

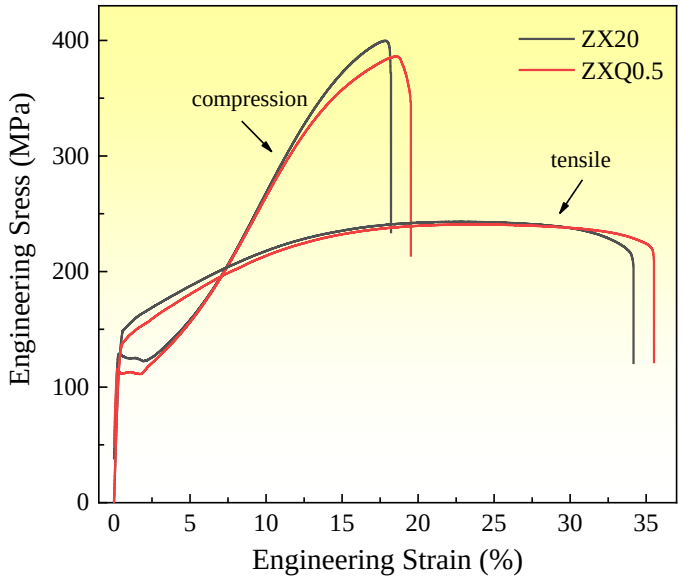

Fig. 7. Tensile and compressive stress-strain curves of as-extruded ZX20 and ZXQ0.5 alloys.

Table 4 TYS, UTS, EF, CYS, UCS, and FS of as-extruded Mg-2Zn-0.2Ca-xAg (x=0, 0.1, 0.3 and 0.5 wt.%) alloys.

Alloys	Tension			Compression		
	TYS (MPa)	UTS (MPa)	FE (%)	CYS (MPa)	UCS (MPa)	FS (%)
ZX20	151.5 ± 6.2	244.1 ± 2.8	29.9 ± 0.9	107.0 ± 11.2	361.8 ± 13.0	18.6 ± 0.8
ZXQ0.1	144.1 ± 7.0.	239.7 ± 3.2	30.4 ± 1.6	106.1 ± 9.7	373.7 ± 16.8	19.6 ± 1.3
ZXQ0.3	143.3 ± 5.6	239.4 ± 1.3	28.7 ± 2.3	106.4 ± 5.7	371.8 ± 19.4	20.7 ± 1.9
ZXQ0.5	135.8 ± 3.0	239.3 ± 1.1	29.8 ± 2.9	108.1 ± 3.9	381.9 ± 7.8	21.1 ± 2.2

The fracture morphology of the four alloys after tensile tests is illustrated in Fig. 8. Abundant dimples, indicative of ductile fracture, were clearly observed, contributing to the outstanding elongation of the studied alloys (Fig. 7). The secondary phase particles

participated in the dimpling process, as revealed by closer examination of the dimples (Fig. 8(e-h)). Actually, it has been documented that the micro-voids preferably nucleated at the interface between the secondary phase and the matrix, the propagation and coalescence of adjacent voids would eventually lead to fracture of the samples [29].

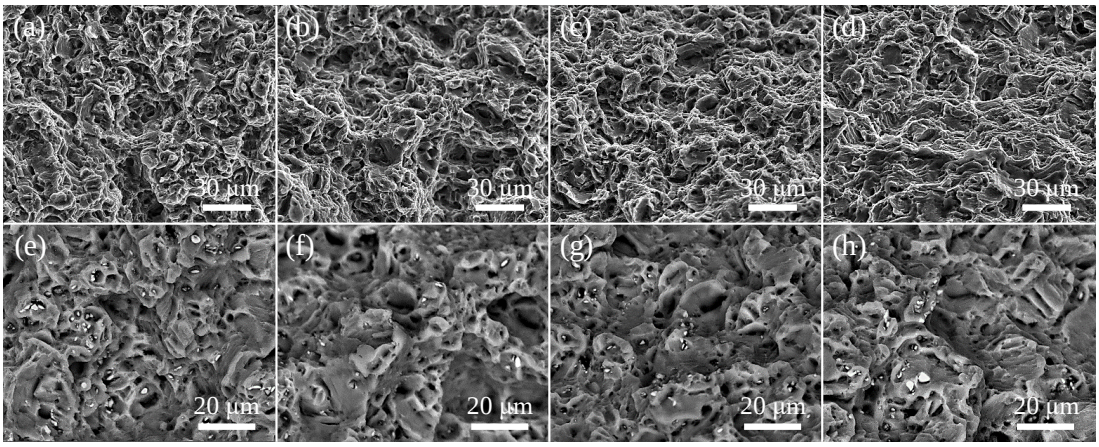

Fig. 8. Second electron images (a~d) and Backscattered electron images (e~h) of tensile-fractured as-extruded Mg-2Zn-0.2Ca-xAg (x=0, 0.1, 0.3 and 0.5 wt.%) alloys: (a, e) ZX20, (b, f) ZXQ0.1, (c, g) ZXQ0.3 and (d,h) ZXQ0.5.

3.3 Immersion tests

The corrosion rates of the samples were assessed by recording hydrogen evolution and weight loss during immersion tests, and the results are illustrated in Fig. 9. As shown in Fig. 9(a), the hydrogen evolution rate (HER) increased within the first 36 hours of immersion, followed by a gradual decrease. Finally, the HER values remained almost unchanged (except for the abrupt HER rise observed from the ZXQ0.5 alloy). This trend could be attributed to the formation and gradual accumulation (and thickening) of corrosion products that partially protect sample surface. Moreover, the HERs noticeably increased with increasing Ag content in the samples. Converting HER values into corrosion rates (mm/y), the Ag-free ZX20 alloy exhibited the slowest corrosion of around 0.35 ± 0.12 mm/y after 15 days' immersion. A minimum addition of 0.1 wt.% Ag dramatically increased corrosion rate to 1.23 ± 0.20 mm/y, which further climbed up to 3.04 ± 0.40 mm/y and 3.13 ± 0.12mm/y when the Ag content increased to 0.3 wt.% and 0.5 wt.%, respectively.

The corrosion rate represented by the weight loss rate (WLR) aligned well with that illustrated by HER. For alloys with Ag content below 0.3%, lower WLR were observed

after the long-term (15 days) immersion compared to the short-term (5 days) one. However, an inversed WLR trend was observed from the ZXQ0.5 alloy, where a higher WLR was recorded after 15 days' immersion (Fig. 9(b)). The corrosion rates (P_W) of as-extruded alloys, converted from the WLR, were 0.40 ± 0.23 mm/y, 1.29 ± 0.38 mm/y, 2.74 ± 0.95 mm/y, and 3.27 ± 0.24 mm/y, for the ZX20, ZXQ0.1, ZXQ0.3 and ZXQ0.5, respectively.

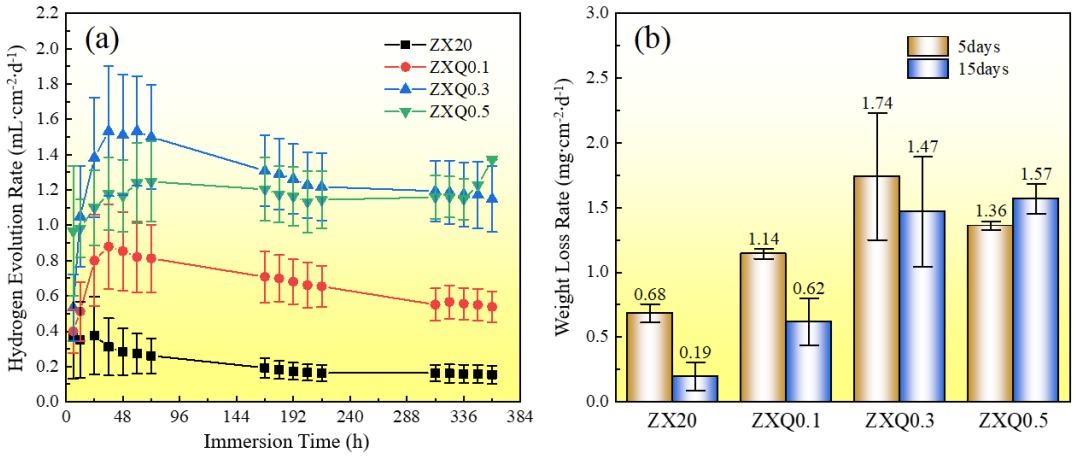

Fig. 9. (a) Hydrogen evolution rate and (b) Weight loss rate of as-extruded Mg-2Zn-0.2Ca-xAg (x=0, 0.1, 0.3 and 0.5 wt.%) alloys immersed in 0.9 wt.% NaCl solution for different times at 37 ± 1°C.

3.4 Electrochemical measurements

Fig. 10 depicts the potentio-dynamic polarization (PDP) curves of as-extruded alloys in a 0.9 wt.% NaCl solution at 37 ± 1 °C. It was clear that the free corrosion potential (E_{corr}) of the sample progressively increased with the increasing Ag content in the alloy, which is consistent with the existing literature [20, 21]. The increased E_{corr} suggested that Ag addition might be beneficial for reducing corrosion susceptibility of Mg-Zn-Ca alloy from the thermodynamics aspect. As expected, all the samples were partially passivated when anodically polarized, possibly due to the accumulation of the corrosion product film on the sample surface [20]. Then passive-active transitions illustrating breakdown of the corrosion film were observed on the anodic branches of PDP curves for all samples. The breakdown potential increased as well with the Ag content. For instance, the breakdown potential of the ZX20 alloy was determined to be -1.56 V *vs*. SCE, while that of the ZXQ0.5 alloy was -1.49 V *vs*. SCE. The stability of the corrosion

film was assessed by the difference between the free corrosion potential (E_{corr}) and the breakdown potential (E_{break}), with the higher potential gap indicating the better stability. From this aspect, the film on ZX20 alloy possessed superior stability as the highest potential gap was determined to be 0.1 V *vs*. SCE from Fig. 10, while the stability of the ZXQ0.5 alloy was the lowest, with a potential difference of 0.08 V.

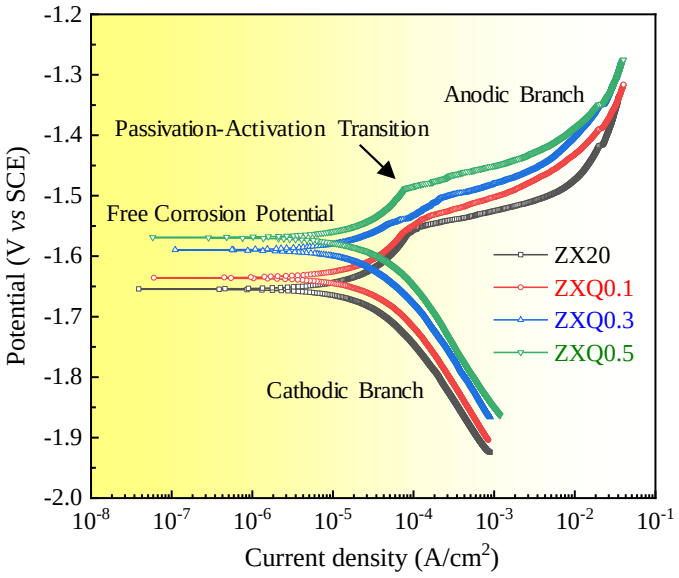

Fig. 10. Potentio-dynamic polarization plots of as-extruded Mg-2Zn-0.2Ca-xAg (x=0, 0.1, 0.3 and 0.5 wt.%) alloys immersed in 0.9 wt.% NaCl solution at 37 ± 1◦C.

Table 5 Fitting results from the PDP plots for as-extruded Mg-2Zn-0.2Ca-xAg (x=0, 0.1, 0.3 and 0.5 wt.%) alloys after immersion for 30 min.

Alloys	E_{corr} (V *vs*. SCE)	B_c (mV/decade)	i_{corr} (μA/cm^2)
ZX20	-1.65 ± 0.01	-199.57 ± 7.15	39.82 ± 3.66
ZXQ0.1	-1.64 ± 0.01	-204.54 ± 5.07	46.54 ± 1.83
ZXQ0.3	-1.60 ± 0.01	-205.83 ± 0.99	48.20 ± 10.86
ZXQ0.5	-1.57 ± 0.01	-229.68 ± 7.19	50.14 ± 7.86

The passive film instability on the Ag-containing alloys led to their deteriorated corrosion resistance. Because the PDP curves did not present any well-defined Tafel region on the anodic branch, the corrosion current density of the alloys were derived through the Tafel extrapolation of the cathodic branches in accordance with that suggested in the literature [30], and the results are summarized in Table 5. The corrosion current density value inversely correlated with the corrosion resistance of the alloys. In this study, the ZX20 alloy exhibited the lowest corrosion current density compared to

the Ag-containing alloys. Moreover, a marginal increase in Ag content was associated with a slight elevation in corrosion current density, indicating a detrimental effect on corrosion resistance due to the addition of Ag to Mg-Zn-Ca alloys. The current density followed the same order as the hydrogen evolution and weight loss rates presented in Fig. 9.

The corrosion behavior of the studied alloys was also evaluated using the electrochemical impedance spectroscopy technique, and the results are presented in Fig. 11. The Nyquist plots (Fig. 11(a)) of the studied alloys comprised two capacitive loops in the first quadrant and one inductive loop (with positive imaginary component of the impedance) in the fourth quadrant. The size of these loops shrunk, as Ag content in the alloy increased, suggesting deterioration of the corrosion resistance. When the Ag content was higher than 0.3 wt.%，the capacitive loop in the middle frequency region had shrunk so much that the two capacitive loops could hardly be differentiated. However, its presence could be indirectly verified from the variation of the phase angle Bode plots shown in Fig. 11(b). The capacitive loop at high frequency originated from charge transfer process across the double-layer, and the capacitive loop at middle frequency referred to the mass transfer through the corrosion product. The inductive loop at low frequency was associated with the desorption and adsorption of corrosion by-products from the sample surface [31].

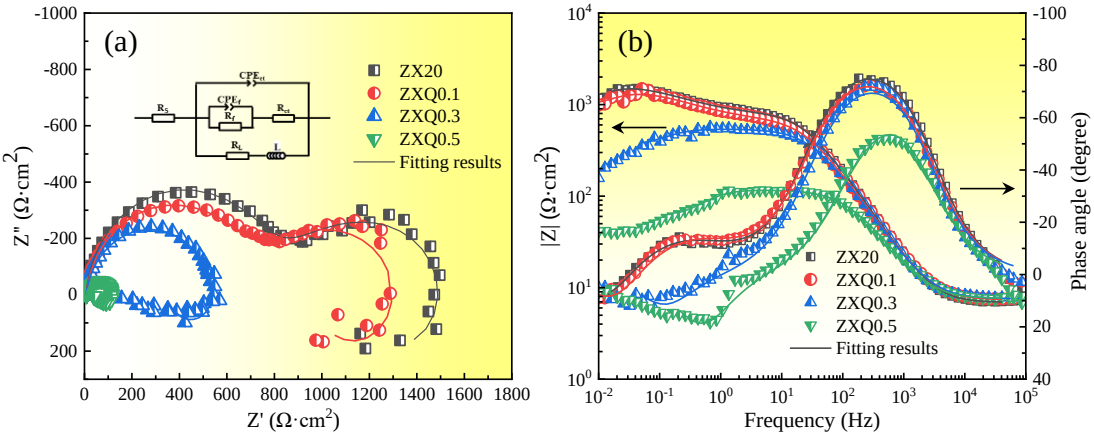

Fig. 11. (a) Nyquist plots and (b) Bode plots of as-extruded Mg-2Zn-0.2Ca-xAg (x=0, 0.1, 0.3 and 0.5 wt.%) alloys immersed in 0.9 wt% NaCl solution at 37 ± 1◦C.

Fig. 11(b) shows the Bode plots for the modulus and phase angle variation as a function

of frequency. The peak in phase-angle Bode plots and the elevation in modulus Bode plots were corresponding to the capacitive loop in Nyquist plots [32]. The first phase-angle peak (at high frequency) was smaller and narrower, and the second phase-angle peak (at low frequency) almost diminished when the Ag addition was ≥0.3 wt.%, suggesting Ag addition was not helpful for the formation of protective film on the surface of studied alloys. The impedance modulus |Z| of all samples coincided quite well in the high frequency domain (10^3-10^5 Hz) because of similar double-layer geometries. As frequency reduced to <10^3 Hz, |*Z*| curves departed from each other, i.e., much lower |*Z*| curves were observed from the Ag-containing alloys. Considering that |*Z*| values were inversely proportional to the corrosion rate of the alloys, it could be inferred that Ag addition compromised the corrosion performance of the Mg-Zn-Ca alloy. The reduced corrosion resistance could be attributed to less protective corrosion films accumulated on the sample surface after comparative analysis of the |Z| values in different frequency domains, which is consistent with the analysis of the PDP curves shown in Fig. 10.

Table 6 Fitting results of EIS data for as-extruded Mg-2Zn-0.2Ca-xAg (x=0, 0.1, 0.3 and 0.5 wt.%) alloys.

Alloys	R_s /Ω·cm^2	R_{ct} /Ω·cm^2	CPE_{ct}-T /μΩ·cm^{-2}·s^n	n_1	R_f /Ω·cm^2	CPE_f-T /μΩ·cm^{-2}·s^n	n_2	R_L /Ω·cm^2	L /H·cm^2	χ^2
ZX20	6.9	786.8	11.7	0.95	996.0	1215.6	0.64	3163.0	45163.0	0.0014
ZXQ0.1	7.3	692.0	14.6	0.93	836.0	1144.7	0.65	2681.0	29394.0	0.0033
ZXQ0.3	7.5	493.2	15.4	0.92	42.0	200.0	0.80	1033.0	1643.0	0.0092
ZXQ0.5	7.6	90.4	19.4	0.92	19.2	185.3	0.81	99.5	47.6	0.0100

An equivalent circuit model shown in Fig. 11(a) was proposed in the present study to quantitatively fitting the EIS results. The physical validation of the equivalent circuit was rationalized by examining cross-sectional morphologies of corroded specimens (shown later). In the circuit, R_s represents the solution resistance, mainly depending on the distance between the working electrode and the Luggin capillary orifice of the reference electrode. Connected in parallel R_{ct} and CPE_{ct} represent the charge transfer resistance and the double layer capacitance of the electrode/solution interface, respectively [32, 33]. The R_f || CPE_f couple analogies impedance associated with the

mass transfer across the corrosion product film [33]. L and R_L in series represent the inductance and its resistance related to the desorption and adsorption of the corrosion products from the corrosion pits.

Using the equivalent circuit, the experimental EIS diagrams were adequately fitted (as verified by the Chi-square χ^2 less than 0.01), and the fitting results were also included as solid lines in Fig. 10. Corresponding fitting parameters are summarized in Table 6. Clearly, both R_{ct} and the R_f decreased dramatically as the Ag content increased in the alloy. R_f and CPE_f-T were closely related with the geometries of the pores in the corrosion film, and larger and thicker pores in the corrosion film normally resulted in lower R_f and CPE_f-T [34]. In this regard and based on the data shown in Table 6, more porous corrosion films might have been accumulated on the alloys with higher Ag contents. Such porous films were unable to provide sufficient protection from corrosion attack, thus, worse corrosion performance was identified in the alloys with higher Ag contents.

3.5 Corrosion morphology

Fig. 12 shows the optical images of as-extruded alloys after being immersed for 5 days in 0.9 wt.% NaCl solution at 37 ± 1 ºC, to uncover their corrosion behavior. The corroded areas increased with immersion time regardless of Ag contents in the alloys. It took approximately 3 hours to visually observe noticeable changes, such as black corrosion filaments on the surface of the Ag-free ZX20 alloy. In contrast, only 1 hour of immersion was sufficient to generate visible changes on the surface of the Ag-containing ZXQ0.1 alloy. This incubation time was further shortened to less than 10 minutes when the Ag content increased to 0.5 wt.%. When the immersion time for the first sight of such changes was taken to evaluate the corrosion resistance of the alloys, a longer duration (raised from the more sustained corrosion product on the surface) indicated better corrosion resistance of the sample with less Ag content. This observation agreed with the breakdown potential analysis of the PDP curves shown in Fig. 10. Moreover, the propagation rate of those initial corrosion sites varied among the samples depending on the Ag content. To be specific, after 3 hours of immersion, the

entire surface of the alloy with more than 0.3 wt.% Ag was badly corroded, while only less than 50% of the surface area of the ZXQ0.1 alloy had been attacked. Therefore, Ag addition to Mg-Zn-Ca alloys may shorten the incubation period of localized corrosion and enhance the corrosion propagation in 0.9 wt.% NaCl solution at 37 ± 1°C.

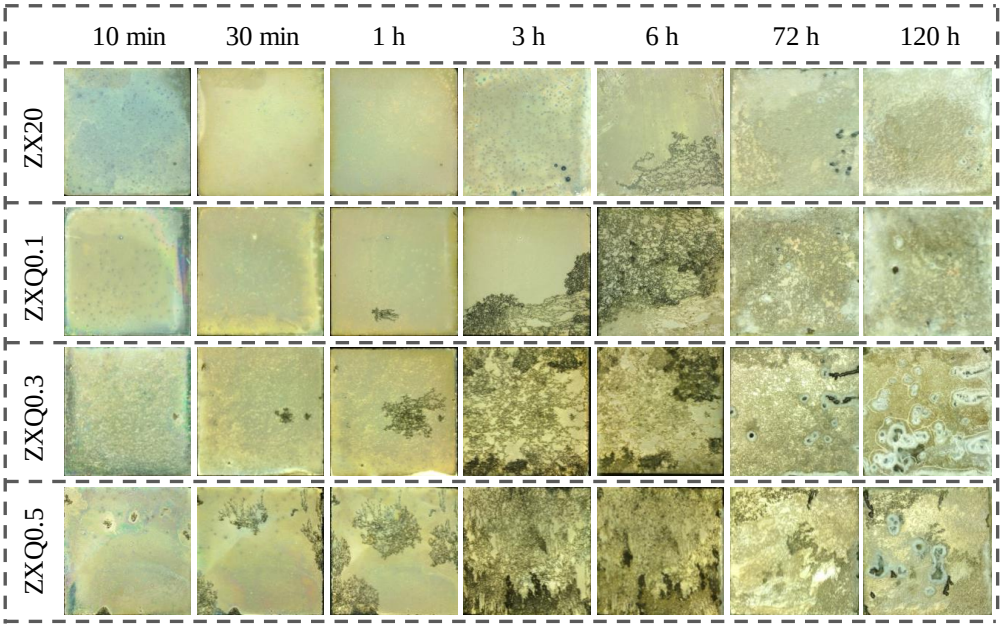

Fig. 12. Optical micrographs showing the surfaces of as-extruded Mg-2Zn-0.2Ca-xAg (x=0, 0.1, 0.3 and 0.5 wt.%) alloys after immersion for various times up to 120 h

Fig. 13 illustrates 3D tomographic maps of the studied alloys after 15-days immersion with the corrosion products removed. The corrosion filaments and pits were visible on the sample surfaces. As Ag content increased to 0.5 wt.%, the localized corrosion area expanded, and its local depth notably increased from 636.4 μm to 1500.9 μm. This outcome suggested an augmented inclination toward vertical corrosion, leading to a deterioration in the corrosion resistance of Ag-containing alloys.

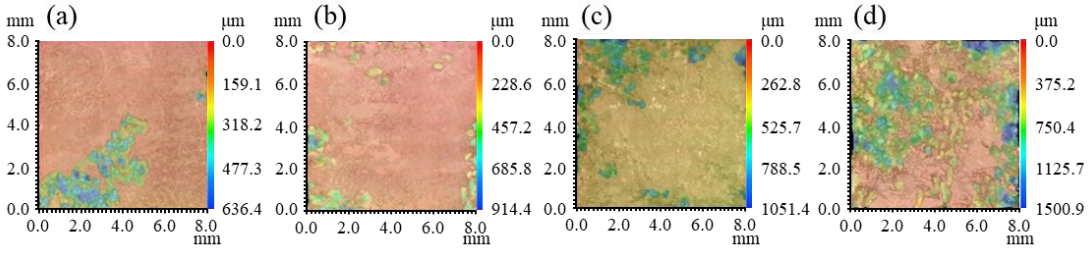

Fig. 13. 3D tomographic maps of as-extruded Mg-2Zn-0.2Ca-xAg (x=0, 0.1, 0.3 and 0.5 wt.%) alloys without corrosion products: (a) ZX20, (b) ZXQ0.1, (c) ZXQ0.3 and (d) ZXQ0.5.

The above analysis provides additional evidence that adding Ag to the ZX20 alloy

significantly compromised its corrosion resistance, particularly when the Ag content exceeded 0.3 wt.%. Fig. 14 displays corrosive morphologies of ZX20 and ZXQ0.5 alloys after immersion for 1 minute, 30 minutes, and 3 hours with the corrosion products removed. Discrete localized corrosion sites were observed on the ZX20 alloy after the initial 30-min immersion. The examination of corroded morphology revealed that corrosion initiated at the vicinity of the secondary phases (marked by yellow arrows in Fig. 14(a)). The signs of filiform corrosion became apparent when the immersion times prolonged to 3 hours. As for the ZXQ0.5 alloy, the footprint of filiform corrosion could be observed shortly after the beginning of immersion test (<1 min), which propagated rapidly to form larger and deeper corrosion pits with extended immersion durations. It was speculated that the addition of Ag accelerated the corrosion process by hastening the onset of pitting corrosion and creating more local corrosion sites. Besides, regardless of the addition of Ag, the ultimate corrosion type manifested as a blend of pitting corrosion vertically and filamentous corrosion horizontally (Fig. 14(c, i)). Such observation was consistent with that depicted in Fig. 12.

Cross-sectional SEM images of the studied alloys after 5 days of immersion in a 0.9 NaCl solution, with corrosion products retained, are displayed in Fig. 15. All alloys were covered by corrosion products, whose morphologies depended on Ag content. To be specific, a relatively uniform product film was formed on the surface of Ag-free alloy with a thickness of ~45 μm, while the product film on Ag-containing alloys was uneven with the maximum thickness up to ~154 μm. Correspondingly, a relatively uniform interface between the substrate and the corrosion film had been observed in the ZX20 alloy, and the surface of ZX20 alloy roughly maintained its integrity except for some discrete corrosion pits expanded deep towards the substrate (Fig. 15(a)). Nevertheless, the scenario was dramatically different when a trace amount (0.1 wt.%) of Ag was added into the alloy. The corrosion product became more porous, and the surface of the substrate was aggressively attacked, leaving some deeper pits (Fig. 15(b)) compared with that observed from the ZX20 alloy.

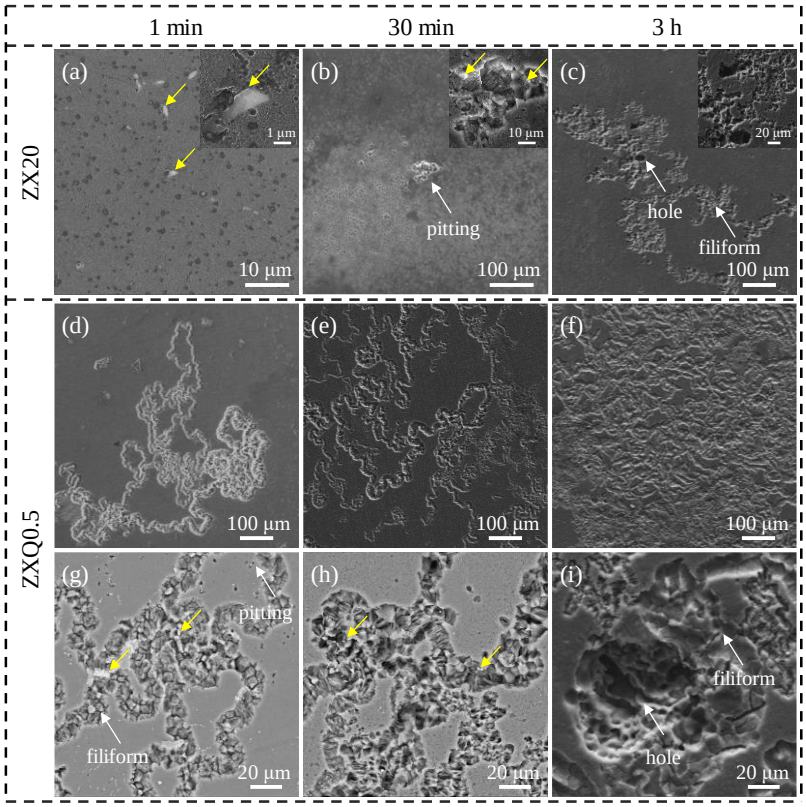

Fig. 14. SEM images without corrosion products of ZX20 and ZXQ0.5 after immersion for various times up to 3 h in 0.9 wt.% NaCl solution at 37 ± 1◦C (Yellow arrows were used to mark the intermetallic).

Further increasing the Ag content in the alloy resulted in a thicker and nonuniform corrosion film, and almost the entire surface of the samples had been corroded. Then corrosion pits propagated even deeper towards the substrate with a maximum pitting depth of around 40 μm being measured in the ZXQ0.3 alloy. Additionally, the corrosion cracks were more evident in the Ag-containing alloys. It was worth noting that the cracks referred to here were not in a straight style alike that formed due to dehydration caused by electron bombardment of specimens during SEM observation, but rather in an irregular form (formed by the lower Pilling-Bedworth ratio of Mg). The porous corrosion film was only loosely attached to the sample surface (consistent with the EIS analysis), through which the corrosion medium easily penetrated towards the substrate to compromise its corrosion resistance. Furthermore, similar to that observed in Fig. 14, the initiation and propagation of corrosion sites around and along the secondary phases is also evident in Fig. 15, suggesting possible occurrence of micro-galvanic corrosion during immersion.

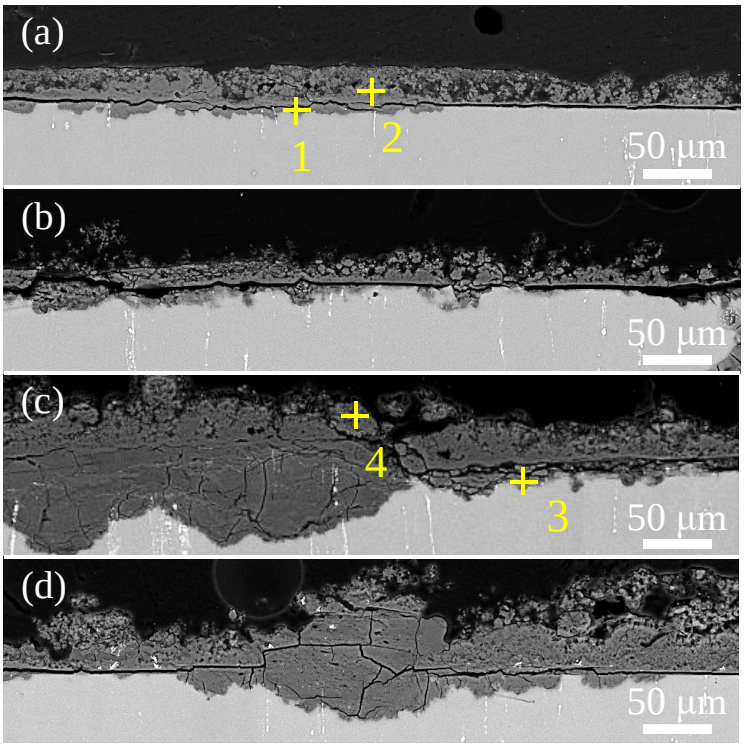

Fig. 15. Cross-section BSE images of as-extruded Mg-2Zn-0.2Ca-xAg (x=0, 0.1, 0.3 and 0.5 wt.%) alloys immersed in 0.9 wt.% NaCl solution for 5 days at 37 ± 1◦C: (a) ZX20, (b) ZXQ0.1, (c) ZXQ0.3 and (d) ZXQ0.5.

Chemical composition of the corrosion film was investigated using EDS technique, and the results are shown in Table 7. Mainly O and Mg were detected from the corrosion film of the studied alloys ZX20 and ZXQ0.3. However, the atomic O to Mg ratio appeared to vary along the thickness of the corrosion film. To be specific, the chemical data obtained near the substrate revealed an atomic O/Mg ratio of roughly 1/1, indicating the presence of MgO. This ratio was significantly increased to around 1.6/1 in the outer layer of the corrosion film, suggesting partial hydration of MgO to form $Mg(OH)_2$.

Table 7 EDS results (at.%) collected from the points marked in Fig. 14.

Elements	ZX20		ZXQ0.3	
	1	2	3	4
O	57.5	61.0	47.1	62.1
Mg	41.7	38.8	52.1	37.8
Zn	0.6	0.1	0.6	0.1
Ca	0.2	0.1	0.2	0.1
Ag	-	-	0.1	0.0

XRD results shown in Fig. 16 confirmed the formation of $Mg(OH)_2$ in the corrosion tests by the presence of characteristic peaks around 2θ=18.6º, 50.8º and 62.0º. Thicker

corrosion film had been formed on the alloys with a higher Ag content (Fig. 14), therefore, diminishing the XRD signals from the substrate. Consequently, the relative intensities of $Mg(OH)_2$ peaks to α-Mg increased in Fig. 16.

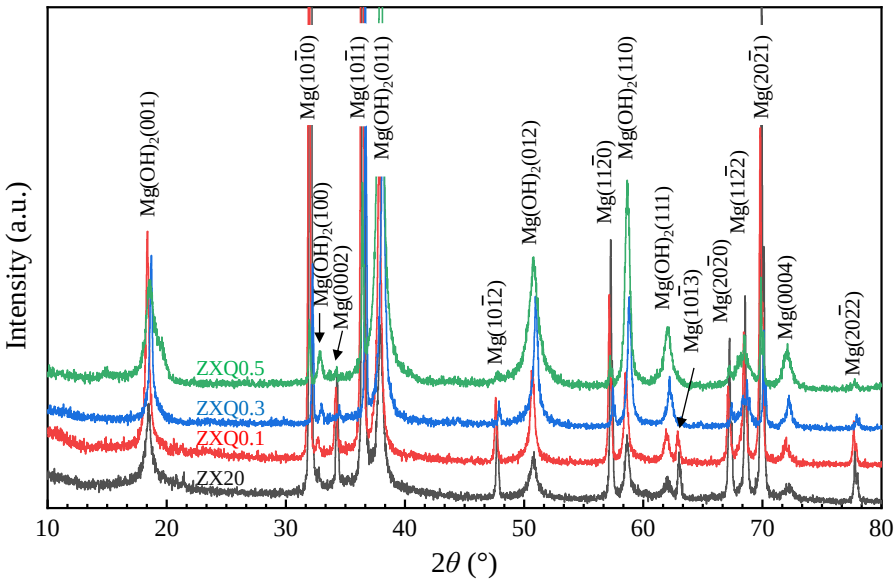

Fig. 16. XRD patterns of surface films on as-extruded Mg-2Zn-0.2Ca-xAg (x=0, 0.1, 0.3, 0.5 wt.%) alloys after immersion in 0.9 wt.% NaCl solution for 15 days.

After characterizing the corroded morphologies of the studied alloys (Fig. 14-15), it became apparent that the corrosion initiated and propagated around the secondary phases. The comparative microstructural characterization (Fig. 1-2) suggested less populous and more refined secondary phases after adding Ag in the Mg-Zn-Ca alloy. The electrode potential variation across secondary phase particles was measured by Kelvin probe technique, and the results are shown in Fig. 17. For the Ag-free ZX20 alloy, the potential difference between the secondary phase and the α-Mg matrix was about 35 mV, whereas incorporating Ag enlarged the value to about 45 mV for the ZXQ0.5 alloy. It is clear that the micro-galvanic couples were more readily formed in the Ag containing alloys because of the larger potential differences. A more refined and populous distribution of the secondary phase in the grain interior of Ag-containing alloys increased the number of micro-galvanic couples, leading to the increased corrosion rates for those alloys.

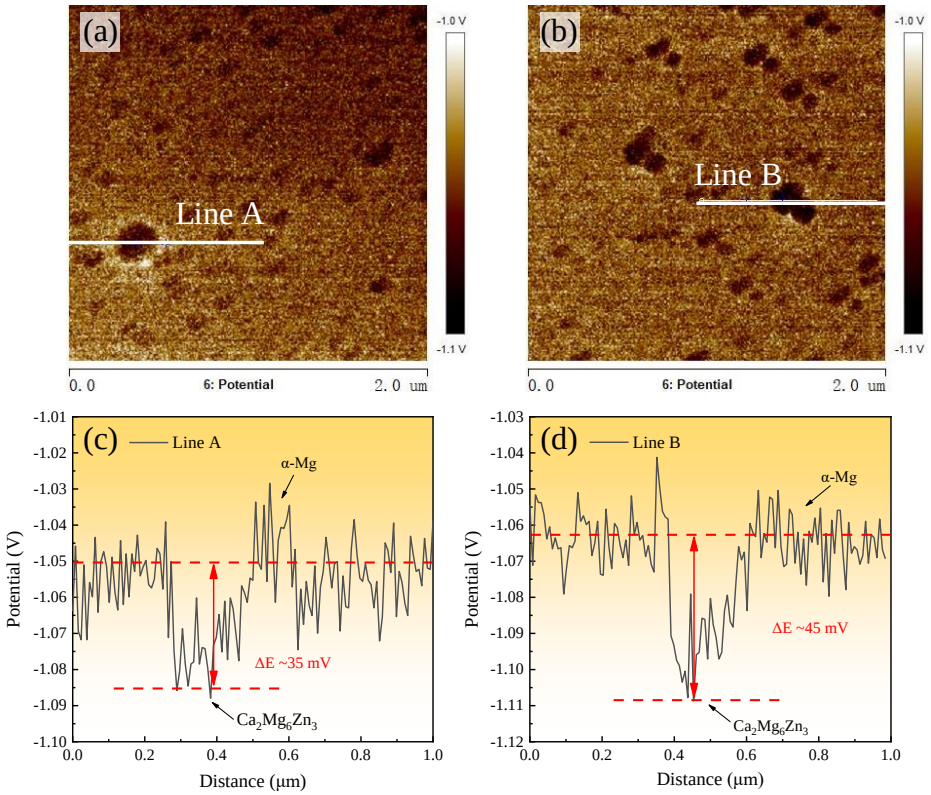

Fig. 17. SKPFM images of as-extruded (a, c) ZX20 alloy and (b, d) ZXQ0.5 alloy: (a, b) surface Volta potential maps and (c, d) corresponding Volta potential profiles

Fig. 18 provides a comprehensive comparison of mechanical properties (fracture elongation) and corrosion resistance of magnesium alloys reported in the literature [8, 18, 31, 35-42]. The present results indicated that a minor addition of Ag to the Mg-Zn-Ca alloy was detrimental to its corrosion resistance while the mechanical properties maintained roughly unchanged. Nevertheless, the corrosion resistance of the studied alloys was still similar to, and in some cases outperformed, the averaged degradation performance of other magnesium alloys including pure Mg, Mg-0.3Sc and Mg-1.4Al-0.4Mn-0.4Ca-0.3Er alloys known for their superior corrosion resistance. As suggested in the literature [43], a temporary implant should possess balanced mechanical properties and corrosion resistance, with UTS > 200 MPa, FE >10%, and the corrosion rate < 7 mm/y. Although the corrosion rate of the Mg-Zn-Ca alloy has been increased by Ag addition, it is still suitable for biomedical applications from the standpoint of degradation and mechanical performance.

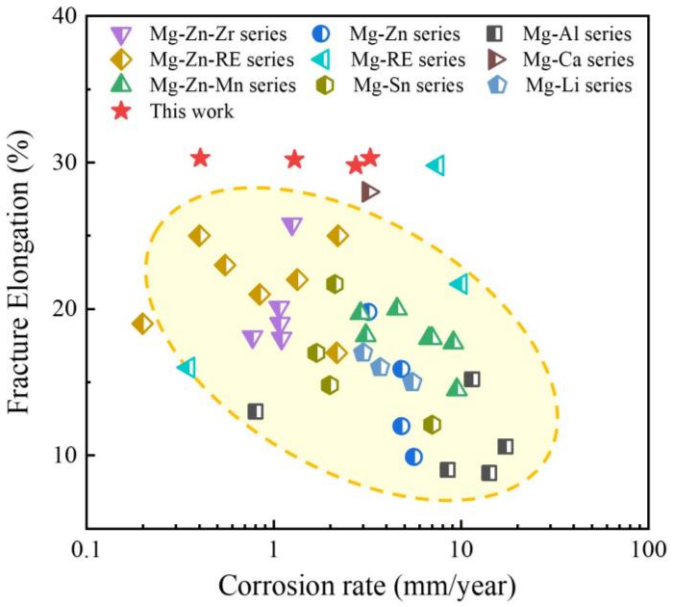

Fig. 18 Elongation to failure of Mg alloys as a function of their corrosion rates [8, 18, 31, 35-42].

Additionally, the studied alloys presented superior ductility compared to other Mg alloys, bringing about additional advantages for biomedical applications associated with increased ease of manufacturing implants with complex geometries (like stents), eliminated risks of brittle fracture to improve the reliability of the bioimplants. Overall, as-extruded Mg-2Zn-0.2Ca-xAg (x=0, 0.1, 0.3, 0.5 wt.%) alloys studied in this work show favorable combination of mechanical and corrosion properties, making them promising materials for biodegradable implants.

4. Conclusions

The effects of Ag addition on the microstructure, mechanical properties as well as corrosion performance of as-extruded Mg-2Zn-0.2Ca (wt.%) alloy were comprehensively studied. The following conclusions could be drawn:

(1) The microstructure of Mg-2Zn-0.2Ca alloy remains almost unchanged with Ag addition even though Ag promotes dynamic recrystallization, refines the secondary phase and reduces its volume fraction. Consequently, all studied alloys exhibited roughly similar mechanical strength, i.e., TYS of ~140 MPa and UTS of ~240 MPa and exceptional fraction elongation of ~30%.

(2) Ag addition enlarged the electrode potential difference between the nobler secondary phase and the α-Mg matrix, which, together with a less stable corrosion film

covering the sample surface, resulted in corrosion resistance progressively deteriorating with increasing Ag content.

(3) The ZX20 alloy possessed the lowest corrosion rate (0.40 ± 0.23 mm/y) compared with the Ag-containing counterparts, and an eight-fold higher corrosion rate (3.27 ± 0.24 mm/y) was observed for the alloy containing 0.5 wt.% Ag.

(4) The corrosion performance as well as the mechanical properties of the Ag-containing Mg-2Zn-0.2Ca alloy exceeded most other Mg alloys. Therefore, it is worth exploring further its feasibility for biodegradable implants.

Data availability statement

The raw and processed data required to support the findings will be made available from the authors upon reasonable request.

Originality statement

The authors confirm that the article has not been submitted to peer review, nor has been accepted for publishing in another journal. The authors also confirm that the research in this work is original, and that all the data given in the article are real and authentic. If necessary, the article can be recalled, and errors corrected.

Acknowledgements

The work was financially supported by the Natural Science Foundation of Hunan Province (Grant No. 2023JJ30673). DG appreciates the support from the UKRI MRC Future Leaders Fellowship (Grant No. MR/T019123/2) and Royal Society International Exchanges 2021 Cost Share (NSFC) (Grant No. IEC\NSFC\211323).

References

[1] J. Wang, J. Dou, Z. Wang, C. Hu, H. Yu, C. Chen, Research progress of biodegradable magnesium-based biomedical materials: A review, J. Alloy. Compd., 923 (2022) 166377.

[2] M.S. Silva-López, L.E. Alcántara-Quintana, The Era of Biomaterials: Smart Implants?, ACS Appl. Bio Mater., 6 (2023) 2982-2994.

[3] H. Roh, J. Park, S. Lee, D. Kim, G. Lee, H. Jeon, M. Chae, K. Lee, J. Sun, D. Lee, H. Han, Y. Kim, Optimization of the clinically approved Mg-Zn alloy system through the addition of Ca, Biomater. Res., 26 (2022) 41.

[4] P. Kumar Rout, S. Roy, D. Rathore, Recent advances in the development of Mg-Ca-Zn alloys as biodegradable orthopedic implants, Mater. Today Proc., (2023).

[5] D. Ma, S. Luan, P. Jin, L. Sun, J. Wang, The effects of Ca on the microstructure, mechanical and corrosion properties of extruded Mg–2Zn–0.5Mn alloy, J. Mater. Res. Technol., 25 (2023) 2880-2889.

[6] N.G. Sommer, D. Hirzberger, L. Paar, L. Berger, H. Ćwieka, U.Y. Schwarze, V. Herber, B. Okutan, A.J. Bodey, R. Willumeit-Römer, B. Zeller-Plumhoff, J.F. Löffler, A.M. Weinberg, Implant degradation of low-alloyed Mg–Zn–Ca in osteoporotic, old and juvenile rats, Acta Biomater., 147 (2022) 427-438.

[7] J. Song, Y. Gao, C. Liu, Z. Chen, The effect of Sr addition on the microstructure and corrosion behaviour of a Mg-Zn-Ca alloy, Surf. Coat. Technol., 437 (2022) 128328.

[8] Y.Z. Ma, C.L. Yang, Y.J. Liu, F.S. Yuan, S.S. Liang, H.X. Li, J.S. Zhang, Microstructure, mechanical, and corrosion properties of extruded low-alloyed Mg-xZn-0.2Ca alloys, Int. J. Miner. Metall. Mater., 26 (2019) 1274-1284.

[9] R.E. Schäublin, M. Becker, M. Cihova, S.S.A. Gerstl, D. Deiana, C. Hébert, S. Pogatscher, P.J. Uggowitzer, J.F. Löffler, Precipitation in lean Mg–Zn–Ca alloys, Acta Mater., 239 (2022) 118223.

[10] L. Zhao, C. Wang, J. Chen, H. Ning, Z. Yang, J. Xu, H. Wang, Development of weak-textured and high-performance Mg–Zn–Ca alloy sheets based on Zn content optimization, J. Alloy. Compd., 849 (2020) 156640.

[11] R. Kumar, P. Katyal, Effects of alloying elements on performance of biodegradable magnesium alloy, Mater. Today Proc., 56 (2022) 2443-2450.

[12] Q. Kang, H. Jiang, Y. Zhang, Z. Xu, H. Li, Z. Xia, Effect of various Ca content on microstructure and fracture toughness of extruded Mg-2Zn alloys, J. Alloy. Compd., 742 (2018) 1019-1030.

[13] X. Qian, Y. Gao, Z. Dong, B. Jiang, C. He, C. Wang, A. Zhang, B. Yang, C. Zheng, F. Pan, The enhanced Zn and Ca co-segregation and mechanical properties of Mg–Zn–Ce alloy with micro Ca addition, Mater. Sci. Eng., A, 867 (2023) 144712.

[14] L. Dragomir, I. Antoniac, V. Manescu, A. Antoniac, M. Miculescu, O. Trante, A. Streza, C.M. Cotruț, D.A. Forna, Microstructure and Corrosion Behaviour of Mg-Ca and Mg-Zn-Ag Alloys for Biodegradable Hard Tissue Implants, in: Crystals, 2023.

[15] M. Mohammadi Zerankeshi, R. Alizadeh, Ag-incorporated biodegradable Mg alloys, Materialia, 23 (2022) 101445.

[16] X. Wang, Y. Huang, L. Yang, Y. Liu, C. Wang, E. Guo, Effects of Ga/Ag addition on corrosion behavior, cytotoxicity, and antibacterial activity of biodegradable Mg–2Zn alloy, J. Mater. Res. Technol., 29 (2024) 3144-3155.

[17] M. Ramya, K.R. Ravi, Biodegradable nanocrystalline Mg-Zn-Ca-Ag alloys as suitable materials for orthopedic implants, Mater. Today Proc., 58 (2022) 721-725.

[18] H. Zhao, L.Q. Wang, Y.P. Ren, B. Yang, S. Li, G.W. Qin, Microstructure, Mechanical Properties and Corrosion Behavior of Extruded Mg-Zn-Ag Alloys with Single-Phase Structure, Acta Metall. Sin., 31 (2018) 575-583.
[19] D. Zhang, C. Liu, S. Jiang, Y. Gao, Y. Wan, Z. Chen, Effects of trace Ag on the dynamic recrystallization and mechanical properties of Mg-Gd-Y-Zr alloy, Mater. Sci. Eng., A, 880 (2023) 145377.
[20] L. Yu, Z. Zhao, C. Tang, W. Li, C. You, M. Chen, The mechanical and corrosion resistance of Mg-Zn-Ca-Ag alloys: the influence of Ag content, J. Mater. Res. Technol., 9 (2020) 10863-10875.
[21] Y.J. Nie, J.W. Dai, X.B. Zhang, Effect of Ag Addition on Microstructure, Mechanical and Corrosion Properties of Mg-Nd-Zn-Zr Alloy for Orthopedic Application, Acta Metall. Sin.-Engl. Lett., 36 (2023) 295-309.
[22] Y.Z. Ma, D.X. Wang, H.X. Li, C.L. Yang, F.S. Yuan, J.S. Zhang, Microstructure, mechanical properties and corrosion behavior of quaternary Mg-1Zn-0.2Ca-xAg alloy wires applied as degradable anastomotic nails, Trans. Nonferrous Met. Soc. China, 31 (2021) 111-124.
[23] A. Atrens, X. Chen, Z. Shi, Mg Corrosion—Recent Progress, Corros. Mater. Degrad., 3 (2022) 566-597.
[24] M. Bian, X. Huang, Y. Chino, Solute segregation assisted grain boundary precipitation and its impact to ductility of a precipitation-hardenable magnesium alloy, Mater. Sci. Eng., A, 819 (2021) 141481.
[25] W. Sun, Y. Deng, H. Zhan, X. Zhou, Y. Yao, W. Liu, G. Zeng, Interaction of dynamic precipitation and dynamic recrystallization of a Mg-4Sn-3Al-1Zn alloy during hot compression, J. Alloy. Compd., 970 (2024) 172434.
[26] M.R. Barnett, M.D. Nave, A. Ghaderi, Yield point elongation due to twinning in a magnesium alloy, Acta Mater., 60 (2012) 1433-1443.
[27] Y.T. Tang, R. Reiff-Musgrove, W. Gu, J.E. Campbell, M. Burley, J. Dean, T.W. Clyne, Tensile-compressive asymmetry in extruded AZ31B rod and its effect on Profilometry-based Indentation Plastometry (PIP), Mater. Sci. Eng., A, 848 (2022) 143429.
[28] H. Wang, W. Chen, W. Zhang, D. Fang, S. Wang, W. Wang, Improving the tension-compression asymmetry of ZK61 magnesium alloy through texture optimization in combined extrusion, Mater. Charact., 207 (2024) 113599.
[29] H. Pouraliakbar, A. Howells, M. Gallerneault, V. Fallah, Fracture behavior of a rapidly solidified thin-strip continuous cast AA5182 Al-Mg alloy with the Portevin-Le Chatelier effect under varying strain rates, J. Alloy. Compd., 971 (2024) 172810.
[30] G.-L. Song, A. Atrens, Recently deepened insights regarding Mg corrosion and advanced engineering applications of Mg alloys, J. Magnes. Alloy., 11 (2023) 3948-3991.
[31] K. Zhang, C. Wang, D.-W. Wang, M.-X. Li, Y.-L. Ma, Z.-M. Hua, L.-Y. Zhang, J. Li, H.-Y. Wang, Effects of solute redistribution during heat treatment on micro-galvanic corrosion behavior of dilute Mg-Al-Ca-Mn alloy, Corrosion Sci., 213 (2023) 110971.
[32] B. Wang, M. Li, Y. Li, Y. Wang, Y. Gao, H. Wang, Effect of Al/Mn ratio on corrosion behavior of lean Mg-Zn-Ca-Al-Mn alloy processed by twin-roll casting, Corrosion Sci., 212 (2023) 110938.
[33] Q. Xie, A. Ma, J. Jiang, H. Liu, Z. Cheng, Y. Gu, Tailoring the corrosion behavior and mechanism of AZ31 magnesium alloys by different Ca contents for marine application, Corrosion Sci., 192 (2021) 109842.

[34] Y. Gao, A. Yerokhin, A. Matthews, Effect of current mode on PEO treatment of magnesium in Ca- and P-containing electrolyte and resulting coatings, Appl. Surf. Sci., 316 (2014) 558-567.
[35] W.T. Li, X. Liu, Y.F. Zheng, W.H. Wang, W. Qiao, K.W.K. Yeung, K.M.C. Cheung, S.K. Guan, O.B. Kulyasova, R.Z. Valiev, In vitro and in vivo studies on ultrafine-grained biodegradable pure Mg, Mg-Ca alloy and Mg-Sr alloy processed by high-pressure torsion, Biomater. Sci., 8 (2020) 5071-5087.
[36] Z. Zhang, J. Xie, J. Zhang, H. Dong, S. Liu, X. Zhang, J. Wang, R. Wu, Simultaneously improving mechanical and anti-corrosion properties of extruded Mg-Al dilute alloy via trace Er addition, J. Mater. Res. Technol., 150 (2023) 49-64.
[37] W. Ci, X. Chen, Y. Sun, X. Dai, G. Zhu, D. Zhao, F. Pan, Effect of Zn on mechanical and corrosion properties of Mg-Sc-Zn alloys, J. Mater. Res. Technol., 158 (2023) 31-42.
[38] X. Wang, Z. Chen, E. Guo, X. Liu, H. Kang, T. Wang, The role of Ga in the microstructure, corrosion behavior and mechanical properties of as-extruded Mg–5Sn–xGa alloys, J. Alloy. Compd., 863 (2021) 158762.
[39] C. Li, Y. He, H. Huang, Effect of lithium content on the mechanical and corrosion behaviors of HCP binary Mg–Li alloys, J. Magnes. Alloy., 9 (2021) 569-580.
[40] L. Xin, J. Zhou, D. Mei, P. Du, H. Qin, M. Bai, M. Liu, Y. Sun, S. Zhu, S. Guan, Effects of Sc on microstructure, mechanical properties and corrosion behavior of Mg-0.5Zn-0.5Nd-xSc alloys, J. Alloy. Compd., 934 (2023) 168044.
[41] Y. He, R. Wang, L. Yang, L. Yang, H. Liu, X. Wang, C. Peng, Y. Feng, Influence of Sc on the microstructure, degradation behavior, biocompatibility in vitro and mechanical property of Mg-2Zn-0.2Zr alloy, Mater. Des., 221 (2022) 110863.
[42] T. Nakata, C. Xu, H. Yamato, L. Geng, S. Kamado, Effect of microalloyed Al and Ca on mechanical properties and corrosion resistance of high-speed extruded Mg-2Zn-1Mn (mass%) alloy, Mater. Charact., 191 (2022) 112121.
[43] D. Bairagi, S. Mandal, A comprehensive review on biocompatible Mg-based alloys as temporary orthopaedic implants: Current status, challenges, and future prospects, J. Magnes. Alloy., 10 (2022) 627-669.